Infrared Spectra at a Conical Intersection: Vibrations of Methoxy

ARTICLE *in* THE JOURNAL OF PHYSICAL CHEMISTRY A · MARCH 2012

Impact Factor: 2.69 · DOI: 10.1021/jp2116627 · Source: PubMed

2 AUTHORS:

Jayashree Nagesh
University of Toronto
9 PUBLICATIONS **18** CITATIONS
SEE PROFILE

Edwin L. Sibert
University of Wisconsin–Madison
103 PUBLICATIONS **2,905** CITATIONS
SEE PROFILE

Infrared Spectra at a Conical Intersection: the Vibrations of Methoxy

Jayashree Nagesh and Edwin L. Sibert III[1]

[1]*Department of Chemistry and Theoretical Chemistry Institute University of Wisconsin-Madison, Madison, Wisconsin 53706**

(Dated: February 15, 2012)

The $J = 0$ infrared spectrum of methoxy is theoretically calculated for the ground $\tilde{X}^2E$ state using a quartic potential energy force field and quadratic dipole moment expansion, calculated *ab initio* at the CCSD(T) level of theory and cc-pVTZ basis. Writing these expansions with vibronic operators whose symmetry properties are defined with respect to C_{3v} rotation, greatly simplify these calculations. With minor adjustments to the force field, excellent agreement with experiment is found both for the transition energies of CH_3O as well as those of CD_3O. The role of Jahn-Teller and Fermi coupling is illustrated by scaling these terms by a parameter δ that varies from zero to one. Plotting the eigenvalues as a function of δ yields a correlation diagram connecting the harmonic eigenvalues to those of the fully coupled problem. The spectrum for CH_3O is determined using a combination of Davidson and Lanczos iteration schemes. The spectral features are found to be dominated by Jahn-Teller effects, but direct Fermi coupling and indirect potential couplings have important roles. The origin of the complexities in the CH stretch region are discussed.

I. INTRODUCTION

Open shell systems are important in both combustion and atmospheric chemistry. The spectral analysis of these systems is, however, complicated by the myriad of couplings that influence their dynamics and reactivity. In this paper we report theoretical calculations on the infrared spectrum of methoxy, a molecule that continues to be subject of both experimental[1–11] and theoretical studies.[12–15] Its vibrational spectrum is strongly influenced by Jahn-Teller coupling,[11,13,15–18] spin-orbit interactions,[18,19] and Fermi resonances. Our work is motivated by the work of Han *et al.*[11] who have obtained the jet cooled infrared (IR) spectrum of methoxy in the CH stretch region and report on the difficulties of making spectral assignments. For a full discussion of the successes and challenges of the spectroscopy of Jahn-Teller coupled molecules the reader is referred to the review article by Barckholtz and Miller.[20]

In a previous paper[21], hereafter referred to as Paper I, we calculated the eigenvalues of the low lying vibronic states of the methoxy molecule. Calculating the potential surfaces in the vicinity of a conical intersection is an active research area in which there has been considerable progress as of late.[22,23] The high symmetry of methoxy molecule allows one to tackle this problem in a diabatic representation.[18,24] An important feature of Paper I was calculating the Jahn-Teller force field with single reference *ab initio* methods. We demonstrated that the force field, obtained by fitting points of C_s symmetry, accurately describes the *ab initio* potential in regions of lower C_1 symmetry. Using this force field, a variational calculation was performed in the diabatic electronic basis. The results compared well to experiment, the largest exception being that the rocking vibrations are systematically overestimated for both MP2 and CCSD(T) levels of theory.

As a first step towards determining the IR spectrum, dipole moment functions are calculated. Since two potential energy surfaces are involved, the dipole moments must be expressed as vibronic operators. We do this using 'artificial' angular momentum operators for the electronic degrees of freedom. These operators were introduced by Hougen[25] in his study of the double group symmetry properties of Jahn-Teller systems such as methoxy. Using the appropriate projections, the expansion coefficients of the dipole moment expansion can be determined *ab initio*. The vibronic dipole moment expansion is combined with a force field, that is slightly adjusted to bring theoretical and experimental transition energies into excellent agreement. The adjusted force field is tested for CD_3O, and good agreement with experiment is found. Plotting the vibronic eigenvalues as a function of the size of anharmonic vibronic coupling terms yields a correlation diagram. This diagram elucidates the difficulties of assigning the vibronic states in CD_3O. Using the fit surface and calculated dipoles we use iterative methods to evaluate the IR spectrum of methoxy. We discuss the major features of the spectrum and describe the challenges of calculating the spectrum in the CH stretching region.

The organization of this paper is as follows. In Sec. II we provide the theoretical background for the paper. We review the transformation properties of the vibronic operators and use these properties to describe how we calculate the potential and dipole operators. The Hamiltonian operator and basis functions are presented as are the iterative methods for calculating spectra. The calculated transition energies, vibrational assignments, and spectrum are presented and discussed in Sec. III. Our main conclusions are summarized in Sec. IV.

II. THEORY

Our calculation of the IR spectrum of methoxy includes several key steps. The first is the calculation of the potential and dipole surfaces. Second is the construc-

tion of the kinetic energy operator, a description of the basis functions, and an evaluation of the eigenvalues and spectrum. Third is the refinement of the potential force constants to yield a modified potential expansion.

A. Potential and Dipole Expansions

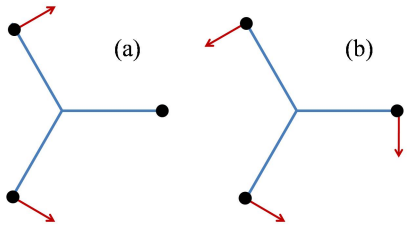

FIG. 1. Plot of one of the three e mode vibrations of methoxy. The molecule is viewed along the OC bond. For $\{S_x, S_y\} = \{0, 0\}$ the molecule has C_{3v} symmetry. The arrows in (a) and (b) correspond to motion along the S_x and S_y coordinates, respectively. Motion along S_x reduces the molecular symmetry to C_s.

The theory of Jahn-Teller coupling for a molecule with the symmetry of methoxy can be found in the third of Herzberg's famous books.[26] Our derivation of the Hamiltonian operator follows the ideas presented there. Using the three-fold symmetry properties of the electronic and vibrational operators with respect to rotation about the body-fixed z-axis of methoxy we show that ideas used to generate the potential can be readily extended to calculate the dipole moment operator.

Since the basic symmetry ideas can be illustrated for the case of a closed shell molecule such as $CHCl_3$, we initiate our discussion there. The degenerate Cl-C-Cl bend degrees of freedom $\{S_x, S_y\}$, depicted in the Fig. 1, can be recast in complex form

$$S_\pm = S_x \pm i S_y = S e^{\pm i\theta}. \tag{1}$$

These coordinates transform as

$$\hat{C}_3 S_\pm = \exp[\pm i 2\pi/3] S_\pm. \tag{2}$$

Since the potential transforms as $\hat{C}_3 V = V$ it must take the following form through third order

$$V = \alpha S_+ S_- + \beta \left(S_+ S_+ S_+ + h.c. \right). \tag{3}$$

This compares to the original representation, which takes the less intuitive form

$$V = \alpha (S_x^2 + S_y^2) + \beta \left(S_x^3 - 3 S_x S_y^2 \right). \tag{4}$$

In the vibrational basis $|v, l_{vib}\rangle$, where v is the total vibrational quanta and l_{vib} is the angular momentum, $S_\pm$ couples states that differ by $l_{vib} = \pm 1$. With the $\{S_+, S_-\}$ coordinates it is clear that the Hamiltonian is block diagonal, since only coupling terms with Δl_{vib} being a multiple of three are allowed. The a, e_+, and e_- symmetry blocks correspond to

$$\ell \equiv l_{vib} \pmod 3 \tag{5}$$

taking values of 0, 1, and 2 respectively.

To extend these ideas to methoxy one must include the electronic degrees of freedom. For configurations with $S_y = 0$, the Hamiltonian has C_s symmetry [see Fig. 1], and the electronic adiabatic eigenstates are labeled according to their symmetry labels as $|A'\rangle$ and $|A''\rangle$. Building a diabatic basis with states of these symmetries hides the three-fold molecular symmetry, so in analogy to eq 1 it is common to work with the electronic basis

$$|\pm\rangle = \left[|A'\rangle \pm i |A''\rangle \right] / \sqrt{2}. \tag{6}$$

The $\pm$ corresponds to $\Lambda = \pm 1$.[20] In general these electronic functions are written as $|\Lambda\rangle$.

The $|\pm\rangle$ states are formally coupled via the operators defined as

$$\begin{aligned} \mathscr{L}_+ \mathscr{L}_+ &\equiv |+\rangle\langle -| \\ \mathscr{L}_- \mathscr{L}_- &\equiv |-\rangle\langle +|. \end{aligned} \tag{7}$$

These operators, introduced by Hougen,[25] are called the artificial ladder operators. There are obvious similarities with the traditional angular momentum raising and lowering operators, hence the notation.

The electronic operators transform as

$$\hat{C}_3 \mathscr{L}_\pm = \exp[\pm i 2\pi/3] \mathscr{L}_\pm. \tag{8}$$

Combining these transformation properties with those of the vibrational $S_\pm$ operators allows us to write the Jahn-Teller Hamiltonian to second order as

$$\begin{aligned} V = &\alpha S_+ S_- + \beta \left(\mathscr{L}_+ \mathscr{L}_+ S_+ + h.c. \right) \\ &+ \gamma \left(\mathscr{L}_+ \mathscr{L}_+ S_- S_- + h.c. \right), \end{aligned} \tag{9}$$

since the allowed terms are the only ones for which $\hat{C}_3 V = V$. The β and γ dependent terms correspond to the first and second order Jahn-Teller coupling terms.[20]

As for the closed shell case [see eq 5] when we write the Hamiltonian in the $|\Lambda\rangle|v, l_{vib}\rangle$ basis, the resulting matrix has a, e_+, and e_- symmetry blocks corresponding to

$$\ell \equiv [\Lambda + l_{vib}] \pmod 3 \tag{10}$$

taking values of 0, 1, and 2 respectively.

In order to calculate the numerical values of the coefficients in eq 9 we project this potential onto states that one can calculate *ab initio*. The description of this procedure, and its extension to the calculation of the dipole moment operators is given in the Appendix. Sample plots of the dipole moments, shown in Fig. 2, illustrate the quality of the fits. Here mode 5 corresponds to the doubly degenerate internal rocking motion of the molecule. This and the remaining internal coordinates are described in Table I. The definition of these symmetry coordinates in terms of bond angles and stretches is given in Eq. (15) of Paper I.

TABLE I. Internal coordinates and their symmetries.

mode	symmetry	description
1	a_1	CO stretch
2	a_1	CH stretch
3	a_1	HCH bend
$4_x, 4_y$	e	CH stretch
$5_x, 5_y$	e	HCO rock
$6_x, 6_y$	e	HCH bend

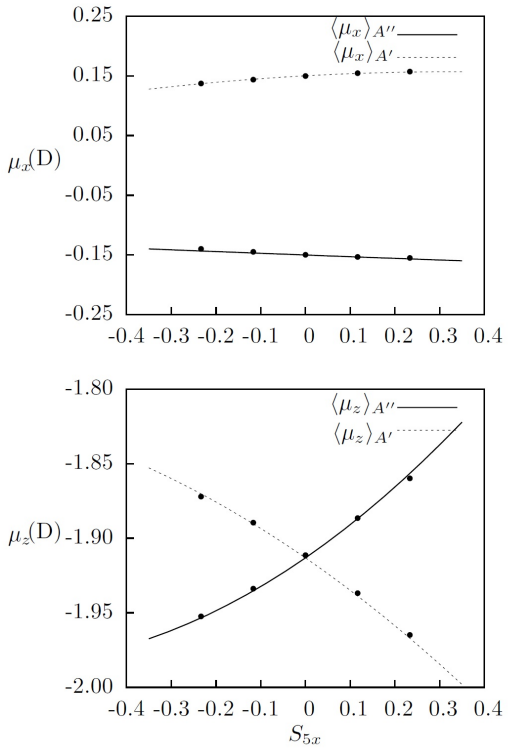

FIG. 2. Plots of the dipole moment components for CH_3O as a function of the symmetry coordinate S_{5x}, with all other coordinates set to 0.0. Lines (dashed or solid) are results of quadratic fits; points are the *ab initio* data using in the fit.

B. Hamiltonian and Basis

Having the potential and dipole in hand we now consider the evaluation of the kinetic energy operator. As the form of this operator is the same as that[27] for closed shell counterparts, such as CHF_3, our description is brief. The kinetic contribution takes the form

$$\hat{K} = \frac{1}{2}\mathbf{P}^T\mathbf{G}\mathbf{P} + V'. \tag{11}$$

We numerically expand the G_{ij} matrix elements through fourth order in the internal coordinates. The potential-like term V' is expanded through second order. Although this kinetic energy operator is not exact, it is calculated to higher order than is the quartic potential.

Combining the kinetic and potential terms we transform the resulting Hamiltonian to a normal mode representation in order to reduce the overall coupling between our basis functions. To obtain these modes, one must be careful about which terms one includes in the quadratic Hamiltonian.

The normal modes are obtained by taking the diagonal quadratic contribution to the potential, i.e., the quadratic terms independent of $\mathscr{L}_+$ and $\mathscr{L}_-$. These terms include

$$V = \frac{1}{2}\sum_{i=1}^{3}\sum_{j=1}^{3} F_{ij}S_iS_j + \frac{1}{2}\sum_{i=4}^{6}\sum_{j=4}^{6} F_{ij}S_{i+}S_{j-}. \tag{12}$$

Rewriting these in terms of the Cartesian components $\{S_{ix}, S_{iy}\}$ yields an **F**-matrix, equivalent in form to the closed shell C_{3v} molecule CHF_3, so one can combine this with the **G**-matrix and follow the standard methods of Wilson, Decius, and Cross[28] to find the normal modes. The resulting frequencies for both CH_3O and CD_3O are shown in Table II. The descriptions, given for CH_3O hold for both species. The one exception is that the CO stretch and the umbrella mode are switched for the deuterated species and are strongly mixed. It should be noted that the descriptions of modes 5 and 6 switch in going from internal to normal coordinates. The fit results will be discussed in Sec. III.

TABLE II. Normal mode frequencies (cm^{-1}) and their symmetries for original CCSD(T) force field and the fit.

		CH_3O		CD_3O		
mode	sym.	CCSD(T)	fit	CCSD(T)	fit	description
1	a_1	2968.0	2967.9	2122.3	2122.2	CH stretch
2	a_1	1435.8	1435.7	1136.3	1134.5	umbrella
3	a_1	1079.6	1076.9	1000.0	998.9	CO stretch
4	e	3042.5	3042.4	2252.6	2252.3	CH stretch
5	e	1458.9	1438.0	1053.8	1041.3	HCH bend
6	e	1096.9	1075.0	851.6	832.7	HCO rock

The internal coordinate Hamiltonian is transformed via a linear transformation to obtain the normal mode representation. Through second order the potential takes the form

$$V = \frac{1}{2}\sum_{i=1}^{3} f_{ii}Q_i^2 + \frac{1}{2}\sum_{i=4}^{6} f_{ii}Q_{i+}Q_{i-}. \tag{13}$$

Following a standard approach, the zeroth order vibronic basis[20] is written in product form

$$|\Lambda,\Sigma\rangle|\mathbf{v},\mathbf{l}\rangle \equiv |\Lambda,\Sigma\rangle|v_1,v_2,v_3,v_4,l_4,v_5,l_5,v_6,l_6\rangle. \tag{14}$$

Here Σ is the spin angular momentum quantum number, $\Lambda = \pm 1$ is the orbital angular momentum of the electron, and v_i is the number of quanta in mode i. For the doubly degenerate modes, l_i denotes the vibrational angular

momentum. The total vibrational angular momentum is $l_{vib} = l_4 + l_5 + l_6$. Using the ℓ symmetry label of eq 10, the matrix representation of the Hamiltonian is block-diagonal with three blocks corresponding to $\ell = 0 - 2$.

To take advantage of the full symmetry for $J \neq 0$, it is essential to symmetrize the basis as[29]

$$\frac{\left[|\Lambda, \Sigma\rangle|\mathbf{v}, \mathbf{l}\rangle \pm (-1)^{\frac{1}{2}-\Sigma}|-\Lambda, -\Sigma\rangle|\mathbf{v}, -\mathbf{l}\rangle\right]}{\sqrt{2}}. \quad (15)$$

For $J = 0$ this matrix representation of the Hamiltonian still contains 3 blocks. However the blocks no longer correspond directly to the three values of the ℓ quantum number. For example the ground state

$$\frac{\left[|+, \frac{1}{2}\rangle|\mathbf{0}, \mathbf{0}\rangle \pm (-1)^{\frac{1}{2}-\Sigma}|-, -\frac{1}{2}\rangle|\mathbf{0}, \mathbf{0}\rangle\right]}{\sqrt{2}}. \quad (16)$$

contains admixtures of $\ell = 1$ states with $\Sigma = \frac{1}{2}$ and $\ell = 2$ states with $\Sigma = -\frac{1}{2}$.

For the $J = 0$ states, Σ is a good quantum number and the $\pm$ linear combinations are degenerate. Consequently the symmetrized and unsymmetrized representations are equivalent even if their ℓ labeling is not. To simplify the labeling of our states we work with the basis of eq 14 with $\Sigma = \frac{1}{2}$ and henceforth drop the Σ label. We will also use the standard short-hand notation for the vibrations, *e.g.* $|4_3^1\rangle$ corresponds to the state with $v_4 = 3$ and $l_4 = 1$. The vibrational function is omitted when we are referring to the ground state.

In comparing to other work, it should be noted that there are two conventions for the sign of l_{vib}. Our work follows that of Hougen,[25] not that of Longuet-Higgins.[30] In comparing to other work, we use the Hougen convention throughout. Barckholtz *et al.*[20] use the following definition of $j^{(k)}$ quantum number

$$j^{(1)} = l_{vib} - \frac{\Lambda}{2}; \quad j^{(2)} = \frac{l_{vib}}{2} + \frac{\Lambda}{2} \quad (17)$$

where k is the order of vibronic Hamiltonian for which $j^{(k)}$ remains a good quantum number. One can readily verify that $j^{(k)}$ is conserved for β ($k = 1$) and γ ($k = 2$) terms of eq 9.

If spin is included in the basis set, a 2π rotation of the basis function returns the function with the opposite phase. Hence the C_{3v} double group must be used. This consideration has lead to the use of the Ω quantum number defined as

$$\Omega = l_{vib} + \Lambda + \Sigma. \quad (18)$$

A vibronic state is classified as $e_{3/2}$ state if $2|\Omega|$ is a multiple of 3, otherwise it is classified as $e_{1/2}$. The lower spin-vibronic basis state of eq 16 therefore is a $e_{3/2}$ state. The $e_{1/2}$ states correspond to both $\ell = 0$ or $\ell = 2$ states. Table III compares the two descriptions for basis states corresponding to fundamental excitation of the CH stretches.

TABLE III. Vibronic basis states corresponding to CH fundamentals with symmetry labels.

basis state	symmetry	ℓ
$\|+\rangle$	$e_{3/2}$	1
$\|-\rangle$	$e_{1/2}$	2
$\|+\rangle\|1_1\rangle$	$e_{3/2}$	1
$\|-\rangle\|1_1\rangle$	$e_{1/2}$	2
$\|+\rangle\|4_1^1\rangle$	$e_{1/2}$	2
$\|+\rangle\|4_1^{-1}\rangle$	$e_{1/2}$	0
$\|-\rangle\|4_1^1\rangle$	$e_{1/2}$	0
$\|-\rangle\|4_1^{-1}\rangle$	$e_{3/2}$	1

III. CALCULATIONS AND RESULTS

The IR spectra are obtained in a three step process.[31] First we calculate the ground state $|\Psi_{gs}^{\ell=1}\rangle$ using the Davidson method.[32] Our initial guess vector is the zero point basis function with $\ell = 1$. We then multiply $|\Psi_{gs}^{\ell=1}\rangle$ with the dipole moment functions to obtain

$$\begin{aligned} |\Psi^{\ell=0}\rangle &= \mu_-|\Psi_{gs}^{\ell=1}\rangle \\ |\Psi^{\ell=1}\rangle &= \mu_z|\Psi_{gs}^{\ell=1}\rangle \\ |\Psi^{\ell=2}\rangle &= \mu_+|\Psi_{gs}^{\ell=1}\rangle \end{aligned} \quad (19)$$

the starting vectors for the Lanczos iterations[33,34] for each of the three symmetry blocks. The overlap squared between the eigenfunctions $|i\rangle$ of the Krylov subspace and the starting vector multiplied by the frequency of the transition gives the intensity of the peaks. The positions are given by the eigenvalues of the Krylov subspace. For example,

$$S(E) = \sum_i E_i|\langle i|\Psi^{\ell=0}\rangle|^2 F(E_i - E) \quad (20)$$

where $F(E)$ is the lineshape. We used Gaussians with a full width half maximum of 1.5 cm^{-1}.

A basis state is included in the Lanczos calculation if

$$7(v_1 + v_4) + 5v_2 + 3v_3 + 4v_5 + 2v_6 \leq v_{\max} \quad (21)$$

where the value of $v_{\max}$ determines the size of the basis. The coefficients in the above equation were determined by trial and error. In general, higher frequency modes are chosen to have higher coefficients, so that basis states of higher energy are not included in the basis. Basis states with high v_6 values were included, since this mode has the greatest Jahn-Teller distortion. No constraints are placed on the vibrational angular momentum values beyond $l_i \leq v_i$.

Increasing $v_{\max}$ from 38 to 54 increases the basis from 39631 to 371100 functions for the $\ell = 0$ calculation. Similar results are found for the other ℓ values. This change in basis leads to a few of the states shown in Table IV

to change by 1-2 cm^{-1}. The time consuming computational step for us is setting up the Hamiltonian; it contains over 16000 terms when expressed in terms of raising and lowering operators. For this reason we do not calculate the matrix on the fly. Instead, we store the non-zero elements and use sparse-matrix methods for the iteration step. Only those matrix elements H_{ij} that satisfy $|H_{ij}|/|H_{ii} - H_{jj}| \geq 10^{-5}$ are retained. Typically no more than 450 iterations are needed for convergence. While more sophisticated approaches are available,[35,36] the current approach sufficed for our purposes. These CCSD(T) energies, labeled $E(ab)$, agree with those of Paper I. There the eigenvalues were obtained using a basis set contraction based calculation applied to the same Hamiltonian.

TABLE IV. Comparison of theoretical and experimental fundamentals (cm^{-1}).

		Experiment				Theory		
ℓ	State	E^{37}	E^{39}	E^{40}	E^{38}	E^{18}	$E(ab)$	E(fit)
2	0_0	62	64	63	63	60	60	61
1	2_1	1365	1371	1373	1360	1445	1376	1373
2	2_1	1413	1418	1417	1428	1489	1402	1415
1	3_1	1043	1047	1060	1047	1112	1049	1045
2	3_1	1107	1111	1126	1110	1182	1116	1107
0	5_1	1344				1443	1374	1344
0	5_1	1433				1511	1461	1433
2	5_1	1517	1521	1526	1519	1571	1529	1516
1	5_1	1523				1581	1540	1521
0	6_1	682	685	686	685	756	705	685
0	6_1	944				1189	973	946
2	6_1	1224				1327	1249	1221
1	6_1	1232			1230	1341	1259	1233

Inspecting Table IV, we see that for the most part the $E(th)$ results are in good agreement with experiment. However, for modes 5 and 6 there are some obvious discrepancies with the experimental work. With minor variations of select linear and quadratic terms we were able to improve the agreement considerably. The improved fits were obtained by calculating the derivatives $\partial E_i(ab)/\partial f_j$ for the CCSD(T) force field and then minimizing

$$\Delta = \sum_{i=1}^{N} [E_i(\text{exp}) - E_i(\text{fit})]^2 + \sum_{j=1}^{M} \sigma \left[\frac{(f_j(ab) - f_j(\text{fit})}{f_j(ab)} \right]^2 \tag{22}$$

where we assume

$$E_i(\text{fit}) = E_i(ab) + \sum_{j=1}^{M} \frac{\partial E_i}{\partial f_j} \left(f_j(\text{fit}) - f_j(ab) \right). \tag{23}$$

We found that the changes in the force field were sufficiently small that the above first order approximation was valid, and it was only necessary to repeat this process once.

The states included in the fit are the stimulated emission pumping data of Temps[37] shown in Table IV. It should be noted that when fitting the $\ell = 1$ and 2 states for modes 5 and 6, there is some ambiguity associated with the state assignment. These states are only split by a few wavenumbers. We assumed the higher energy of the two states to be $\ell = 1$ states, since this ordering was robust in our force field. We were unable to obtain good fits with the reverse ordering. The force constants that are varied are those whose fit values are shown in Table V. The σ dependent term is included to avoid changes in force constants that do not significantly improve the agreement with experiment. For low values of σ, an increase in its value has little effect on Δ. We systematically increased σ to a value of 3000, after which point Δ began to increase rapidly. This was the value used in the minimization. Our fit surface is compared to the original surface in Table V. The changes are minimal; the largest are for mode 5 and 6. The changes in the Jahn-Teller terms caused a decrease in the spin-orbit induced splitting of ground state, so we increased the spin-orbit coupling

$$H_{SO} = -\lambda \left(|+\rangle\langle +| - |-\rangle\langle -| \right), \tag{24}$$

from $\lambda = 60$ to 64 cm^{-1}. The eigenvalues of the Hamiltonian with the fit surface, labeled E(fit), are reported in Table IV. One can see that the agreement is excellent.

TABLE V. Quadratic contribution to internal coordinate force field for the CCSD(T), $F(ab)$, and fit force constants F(fit).

F(ab)	F(fit)[a]	term[b]	$F(ab)$	F(fit)[a]	term[b]
22389		$S_{4+}S_{5-}$	-834		$S_1S_{4+}\mathscr{L}_+\mathscr{L}_+$
-280453		$S_{4+}S_{6-}$	10902		$S_1S_{5+}\mathscr{L}_+\mathscr{L}_+$
357917	339610	$S_{5+}S_{6-}$	13017		$S_1S_{5+}\mathscr{L}_+\mathscr{L}_+$
43254		S_1S_2	237		$S_2S_{4+}\mathscr{L}_+\mathscr{L}_+$
-8503		S_2S_3	1969		$S_2S_{5+}\mathscr{L}_+\mathscr{L}_+$
54196		S_1S_3	414		$S_2S_{6+}\mathscr{L}_+\mathscr{L}_+$
259054	257836	S_1^2	1279		$S_3S_{4+}\mathscr{L}_+\mathscr{L}_+$
155457		S_2^2	-5781		$S_3S_{5+}\mathscr{L}_+\mathscr{L}_+$
33276		S_3^2	-2175		$S_3S_{6+}\mathscr{L}_+\mathscr{L}_+$
151382		$S_{4+}S_{4-}$	943		$S_{4+}S_{4+}\mathscr{L}_-\mathscr{L}_-$
21921	20783	$S_{5+}S_{5-}$	-2614	-2468	$S_{5+}S_{5+}\mathscr{L}_-\mathscr{L}_-$
27419	26867	$S_{6+}S_{6-}$	1457	1477	$S_{6+}S_{6+}\mathscr{L}_-\mathscr{L}_-$
-93		$S_{4+}\mathscr{L}_+\mathscr{L}_+$	1335		$S_{4+}S_{5+}\mathscr{L}_-\mathscr{L}_-$
2536	2528	$S_{5+}\mathscr{L}_+\mathscr{L}_+$	-389		$S_{4+}S_{6+}\mathscr{L}_-\mathscr{L}_-$
-2734	-2883	$S_{6+}\mathscr{L}_+\mathscr{L}_+$	978	976	$S_{5+}S_{6+}\mathscr{L}_-\mathscr{L}_-$

[a] Only altered values are reported.

[b] Complex terms have complex conjugate pairs (not shown).

The fit normal modes are compared to the original normal modes for both CH_3O and CD_3O in Table II. As expected the largest shifts are for modes 5 and 6. As a

test of our potential we consider the eigenvalues of CD_3O. Table VI compares our calculated CD_3O transition frequencies with those obtained by Foster *et al.*[38] with free jet cooled laser induced spectroscopy. The experimental energies are the line displacements (in cm^{-1}) from the pump lines. Each column corresponds to a different pumped band. The spread in the experimental data is due to a combination of the finite resolution of the dispersed fluorescent method, rotational band widths, and the fact that some transitions have low intensity. Overall the agreement between theory and experiment is good, especially in light of the variance in reported transition energies as a function of upper state levels.

TABLE VI. CD_3O $\tilde{X}^2E$ vibrational intervals[a] (in cm^{-1}) observed in dispersed fluorescence[38] compared to E(fit) eigenvalues.

0_0^0	3_0^1	3_0^2	2_0^1	$2_0^1 3_0^3$	$1_0^1 3_0^3$	$5_0^1 3_0^4$	E(fit)	ℓ
56	54	55	57	54	51	52	54	2
516	517	523		520		530	514	0
				722	742	739	721	0
							904	2
915	918	923	920	922	921	919	913	1
948[b]								
					993	995	970	0
				1015[a]			1005	1
1036	1039	1048	1029	1045			1036	2
							1046	1
					1063		1047	0
1083	1086	1093					1087	2
1196	1198	1205	1201	1202	1205	1201	1201	2
							1180	1
							1261	2
				1287		1284	1289	1
							1481	1
1487	1486	1499		1496	1502	1487	1490	2
1609	1606	1617				1625	1607	0

[a] Different experimental columns correspond to different pump bands.

[b] Shoulder.

We have left the spectrum unassigned except for the ℓ quantum number. This is due to mixing of the normal modes states. The extent of this mixing is evident in a correlation plot that connects the eigenvalues of the normal modes, plus spin-orbit coupling, to the eigenvalues of the fully coupled Hamiltonian. This diagram, shown in Fig. 3, was obtained by splitting the Hamiltonian into two contributions: an assignable part, that contains the normal mode quadratic Hamiltonian and spin-orbit H_{SO} coupling, plus a part that contains all remaining contributions multiplied by δ

$$H = H^{HO} + H_{SO} + \delta W_b, \tag{25}$$

where δ varies from 0 to 1. The left hand side of the figure is labeled with the good normal mode quantum numbers. The four ν_6 states are the $|+\rangle|6_1^1\rangle$ and $|+\rangle|6_1^{-1}\rangle$ degenerate pair at 837 cm^{-1} and the degenerate pair $|-\rangle|6_1^{-1}\rangle$ and $|-\rangle|6_1^1\rangle$ shifted upwards by 128 cm^{-1}, twice the spin-orbit coupling.

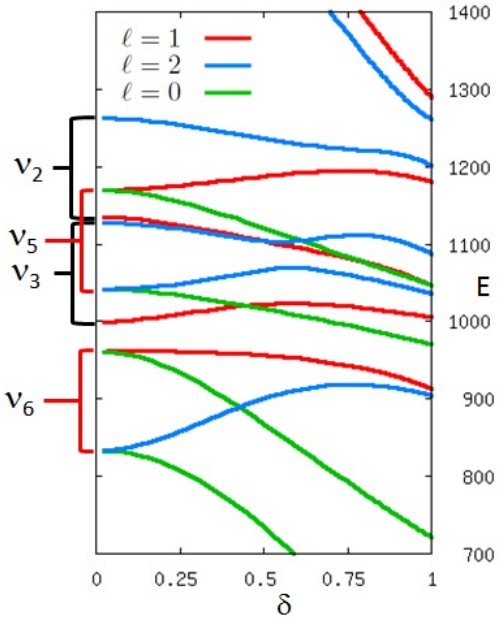

FIG. 3. Correlation diagram for CD_3O as a function of δ.

The fundamentals, i.e. the $v_t \equiv v_2 + v_3 + v_5 + v_6 = 1$ states, are well separated from the $v_t = 2$ states for most of the δ values. Amongst the fundamentals, the $\ell = 0$ states are the only states that can obviously be assigned using the quantum numbers on the left. Some repulsion between $\ell = 1$ states is observed, and substantial repulsion between the $\ell = 2$ is observed, this indicating substantial mixing of these states. For example the red line correlating to the $|+\rangle|3_1\rangle$ for $\delta = 0$ has a .66 $|+\rangle|3_1\rangle$ contribution for $\delta = 1$.

As δ nears a value of one, the overtones of mode 6, seen in the upper right, have dropped sufficiently in energy that they are mixing with the fundamentals, as evidenced by the repulsions in the correlation diagram. This mixing between different manifolds of v_t states becomes profound by the time you consider the mixing between the $v_t = 2$ and $v_t = 3$ states.

The analogous plot to Fig. 3 is shown for CH_3O in Fig. 4. The structure is significantly simpler. The fundamentals, *i.e.* the $v_t = 1$ states are more separated from the $v_t = 2$ states. The CH bending motions of modes 2 and 5 are well separated from the CO stretch and the rocking modes. In addition, in all cases the nearly degenerate states have different ℓ quantum numbers. For example, the three lowest energy states in the figure $\{|+\rangle|6_1^{-1}\rangle, |+\rangle|3_1\rangle, |+\rangle|6_1^1\rangle\}$ have values of $\ell = 0$, 1, and 2 respectively. For the above reasons, the CH_3O

spectrum is easier to assign than is its deuterated analogue.

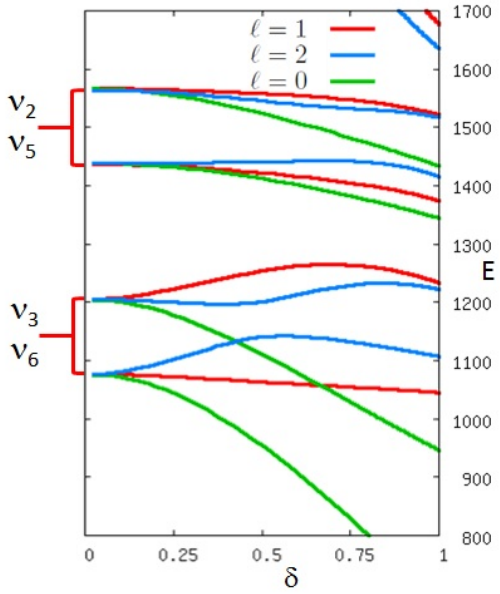

FIG. 4. Correlation diagram for CH_3O as a function of δ.

Having discussed state assignments, the calculated IR spectrum is shown in Fig. 5a Consistent with the correlation diagrams, the spectrum does not display much complexity for the lowest lying states. The combination bands and overtones of the bends show considerable oscillator strength, and there appears to be substantially more state-mixing. The positions and intensities of the transitions are given in Table VII for three different calculations all of which use the fit potential. The 'best' calculation uses a basis determined by $v_{\max} = 50$ of eq 21. This basis has about 223000 functions for each of the ℓ blocks. The intensities are calculated with the dipole moment functions expanded through second order. These intensities are denoted Int(2). These results are compared to the results of a calculation which uses the same dipole but smaller basis. This basis, which is defined using $v_{\max} = 40$, contains 54000 basis. One can see, that with the exception of a few of the higher energy states where there are differences of up to 7 cm^{-1}, there is good agreement between the energies. The absolute intensities are also relatively insensitive to the basis size. Comparing the $n = 2$ to the linear dipole $n = 1$ results, one sees that the linear dipole approximation serves to determine the qualitative features of the spectrum.

The lowest order contributions to the dipole are given in Table VIII. The full quadratic expansion is given in the supplementary material. Noteworthy is the large intensity of the two lowest $\ell = 0$ states. This intensity is mostly due to the pure electronic term $.310\mathscr{L}_+\mathscr{L}_+$. This term acts on the ground state, approximately described as $.83|+\rangle - .43|-\rangle|6_1^{-1}\rangle$ to yield $-0.13|+\rangle|6_1^{-1}\rangle$. This component is entirely due to the first order Jahn-Teller coupling. When higher order contributions to both the ground state wave function and the dipole are considered the value of coefficient decreases from -0.13 to -0.17. This the two $\ell = 0$ eigenstates, which are a_1 and a_2 states in the absences of spin-orbit coupling, are approximately described as $.60|+\rangle|6_1^{-1}\rangle + .49|-\rangle|6_1^{1}\rangle$ and $.49|+\rangle|6_1^{-1}\rangle - .56|-\rangle|6_1^{1}\rangle$ for the lower and higher energy states, respectively. With this simple picture, the intensity for the lower state is calculated as $[(-.17)(.60)]^2 685 = 7.2D^2\text{cm}^{-1}$ which is in qualitative agreement with the result of the Table VIII.

By the time you reach the spectra region of the CH stretch fundamental, see Fig. 5b, the spectrum is congested. As this spectral region has been studied previously,[11] we show it in more detail in the lower panel of the figure. Although there are many lines in this spectrum, its major features can be understood. The starting point of the analysis is the dipole, the salient part of which is

$$\mu_z = .047Q_1 - .037(Q_{4+}\mathscr{L}_+\mathscr{L}_+ + h.c.)$$
$$\mu_\pm = .062Q_1\mathscr{L}_\mp\mathscr{L}_\mp - .057Q_{4\pm} + .036Q_{4\mp}\mathscr{L}_\pm\mathscr{L}_\pm (26)$$

In the absence of Fermi resonances, between the CH stretches and lower frequency modes, the form of the dipole leads to the conclusion that the spectrum should contain 6 peaks corresponding to the 6 fundamentals of Table III. We now discuss the differences between this simple picture and that which is calculated. Our initial discussion highlights those coupling other than the Fermi couplings. Since ℓ is a good quantum number, we use this number to organize our discussion.

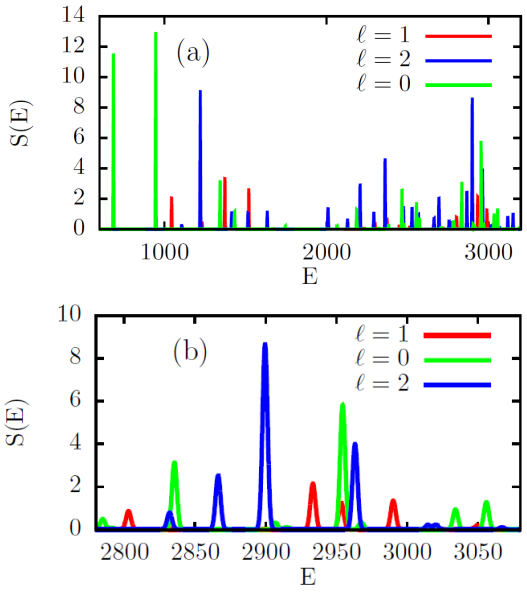

FIG. 5. Infrared spectra for CH_3O obtained using eq 20.

The two largest peaks with $\ell = 0$ roughly correspond to linear combinations of the states $|-\rangle|4_1^1\rangle$ and $|+\rangle|4_1^{-1}\rangle$. While the 100 cm^{-1} splitting of these states is in part due

TABLE VII. Intensities Int$(n)^a$ and transition frequencies E as function of order of dipole expansion, n, and v^b_{max} for fit potential.

	$v_{\max}=50$		$v_{\max}=40$				$v_{\max}=50$		$v_{\max}=40$		
ℓ	E	Int(2)	ΔE^c	Int(2)	Int(1)	ℓ	E	Int(2)	ΔE^c	Int(2)	Int(1)
1	1044.83	2.1	0.02	2.1	2.5	2	2528.06	1.5	0.60	1.5	1.6
1	1232.77	0.4	0.07	0.4	0.3	2	2555.07	1.4	1.13	1.4	1.2
1	1373.27	3.4	0.21	3.4	2.8	2	2567.93	1.1	0.54	1.1	0.9
1	1521.12	2.6	0.23	2.6	1.9	2	2664.29	0.8	0.60	0.8	0.6
1	2009.44	1.3	0.86	1.3	1.1	2	2694.30	2.1	0.62	2.1	1.7
1	2073.84	0.0	0.53	0.0	0.1	2	2757.24	0.6	1.62	0.6	0.8
1	2299.19	0.5	0.63	0.5	0.2	2	2831.90	0.8	6.51	0.8	0.3
1	2373.15	0.7	0.83	0.7	0.1	2	2866.12	2.5	1.50	2.4	1.8
1	2449.42	0.2	0.71	0.2	0.2	2	2899.47	8.7	4.28	8.5	7.4
1	2514.17	0.1	0.77	0.2	0.0	2	2963.04	4.0	2.07	4.3	4.6
1	2528.60	0.5	1.03	0.5	0.2	2	3015.16	0.2	3.59	0.2	0.2
1	2661.29	0.3	0.47	0.3	0.3	0	685.49	11.6	-0.03	11.6	11.5
1	2764.78	0.5	1.40	0.5	0.4	0	946.48	13.0	-0.02	13.0	13.4
1	2803.01	0.9	6.57	0.9	1.2	0	1344.02	3.2	0.12	3.2	3.6
1	2933.43	2.1	3.70	1.8	1.6	0	1433.40	1.2	0.23	1.2	0.9
1	2953.66	1.2	2.02	1.5	0.9	0	1746.18	0.2	0.36	0.2	0.2
1	2990.25	1.4	1.29	1.4	1.6	0	2065.04	0.3	0.63	0.3	0.1
1	3049.83	0.2	1.10	0.2	0.1	0	2186.27	1.3	1.33	1.3	1.4
2	60.93	4.8	-0.01	4.8	4.8	0	2384.17	0.2	0.61	0.2	0.3
2	1106.96	0.2	0.04	0.2	0.3	0	2465.87	2.7	0.68	2.7	2.6
2	1221.84	9.1	0.05	9.2	9.2	0	2477.97	0.3	0.76	0.3	0.4
2	1415.20	1.1	0.28	1.1	1.3	0	2555.51	1.7	0.84	1.7	1.8
2	1516.12	1.2	0.17	1.2	0.9	0	2573.00	0.7	0.99	0.7	0.7
2	1634.76	1.1	0.28	1.1	1.1	0	2784.77	0.5	2.04	0.4	0.5
2	2010.09	1.4	0.85	1.5	1.9	0	2835.46	3.1	4.80	3.2	2.1
2	2130.16	0.6	0.67	0.6	0.4	0	2906.90	0.3	1.34	0.3	0.5
2	2207.98	3.0	0.71	3.0	2.9	0	2954.39	5.8	3.47	5.5	4.4
2	2292.22	1.1	0.54	1.1	0.8	0	2967.54	0.3	2.40	0.6	0.9
2	2362.06	4.7	0.84	4.7	4.8	0	3034.16	0.9	1.20	0.9	1.0
2	2475.47	1.5	0.86	1.5	1.4	0	3056.00	1.3	0.77	1.4	1.3

[a] Intensities calculated using $E_i|\langle i|\mu_\alpha|\Psi^{\ell=1}_{gs}\rangle|^2$ where the α component of the dipole in units of Debye and E_i in units of wavenumbers.

[b] Basis size is determined by $v_{\max}$ (see eq 21).

[c] ΔE is the energy difference between the $v_{\max}=50$ and $v_{\max}=40$ energy.

TABLE VIII. Linear contributions to the dipole moment.

μ_z		μ_+	
coefficient	term	coefficient	term
0.047	Q_1	0.310	$\mathscr{L}_-\mathscr{L}_-$
-0.029	Q_2	-0.057	Q_{4+}
-0.081	Q_3	0.039	Q_{5+}
-0.037	$Q_{4+}\mathscr{L}_+\mathscr{L}_+$	-0.024	Q_{6+}
-0.066	$Q_{5+}\mathscr{L}_+\mathscr{L}_+$	0.063	$Q_1\mathscr{L}_-\mathscr{L}_-$
-0.000	$Q_{6+}\mathscr{L}_+\mathscr{L}_+$	0.032	$Q_2\mathscr{L}_-\mathscr{L}_-$
-0.037	$Q_{4-}\mathscr{L}_-\mathscr{L}_-$	-0.086	$Q_3\mathscr{L}_-\mathscr{L}_-$
-0.066	$Q_{5-}\mathscr{L}_-\mathscr{L}_-$	0.036	$Q_{4-}\mathscr{L}_+\mathscr{L}_+$
-0.000	$Q_{6-}\mathscr{L}_-\mathscr{L}_-$	-0.008	$Q_{5-}\mathscr{L}_+\mathscr{L}_+$
		0.012	$Q_{6-}\mathscr{L}_+\mathscr{L}_+$

to spin-orbit coupling, this alone cannot lead to such a large splitting. In fact, when we repeat the above calculation without the spin-orbit coupling, a large splitting is still observed. When we completely decouple the CH stretches from the lower frequency modes and turn off the spin-orbit coupling, we calculate that the states become nearly degenerate forming an A_1/A_2 doublet. Unlike their rock counterparts that appear around 683 and 944 cm^{-1}, these CH stretch states are only weakly coupled by the Jahn-Teller terms. Clearly the large splitting is due to other terms not yet considered. We find that it is due to multiple, indirect coupling pathways, the most important of which are the below pair

$$|-\rangle|4_1^1\rangle \leftrightarrow |-\rangle|4_1^{-1}6_1^{-1}\rangle \leftrightarrow |+\rangle|4_1^{-1}\rangle$$
$$|+\rangle|4_1^{-1}\rangle \leftrightarrow |+\rangle|4_1^16_1^1\rangle \leftrightarrow |-\rangle|4_1^1\rangle. \quad (27)$$

The outer two CH stretches are coupled to states with an additional quantum of excitation in the rock mode by a purely vibrational $\Delta l_{vib} = 3$ coupling term $Q_{4+}Q_{4+}Q_{6+}$ plus its hermitian conjugate. The second two states are strongly coupled by first order Jahn-Teller coupling, since the middle state has excitation in the rocking mode. The combination of these two couplings is mostly responsible for the observed splitting. An analogous coupling pathway involving mode 5 is also present. This splitting appears to be overestimated in our model, since the lower state is not observed in the Han *et al.* spectrum.[11]

There are expected to be two peaks associated with $\ell = 2$ states due to the μ_+ component of the dipole of eq 26. Both of the zero-order states $|-\rangle|1_1\rangle$ and $|+\rangle|4_1^1\rangle$ carry oscillator strength. These states mix since they are nearly degenerate; the spin-orbit coupling increases the energy of the symmetric stretch state pushing it into resonance with the asymmetric state. Analogous to the above discussed $\ell = 0$ states, there are important indirect coupling pathways between these states. Since both zero-order states carry oscillator strength, one of the peaks tends to gain most of the intensity due to their mixing. This peak is the major feature in our calculated IR spectrum. It probably corresponds to the B band reported by Han *et al.*[11]

Both of the $\ell = 1$ zero-order states $|+\rangle|1_1\rangle$ and $|-\rangle|4_1^{-1}\rangle$ carry oscillator strength due to the μ_z component of the dipole. These states do not mix significantly, since the spin-orbit coupling increases the energy of the already higher energy asymmetric stretch state, pushing it well out of resonance with the symmetric CH stretch state. Based on the rotational selection rules given by Han *el al.*[11] the higher energy bands may correspond to their C and D bands.

The above picture of the coupling is relatively complex, since off-resonance anharmonic CH stretch-bend interactions coupled with Jahn-Teller effects strongly influence the splittings of CH stretch transitions. When one includes the resonant Fermi interactions with the background states, the picture we described above becomes more complex. This finding is consistent with that of Han *et al.*[11] who pointed out that Fermi resonant interactions must be at play. It is easy to understand why there are still considerable differences [*cf.* Marenich and Boggs[18]] between the assigned transition frequencies.[11,37–40] Given the many potential parameters that contribute to the precise positions and intensities of the background states, we have not attempted to vary additional parameters in our Hamiltonian to improve agreement with experiment.[11,37–40]

IV. SUMMARY

In this paper we compared the transition frequencies of CH_3O to experimental works. This comparison highlighted several areas in which our CCSD(T) force field of methoxy could be improved via a fitting procedure. An important aspect of our fit was that the quantity being minimized includes both the sum of the differences between experimental and calculated force constants as well as the sum of the differences between the CCSD(T) force constants and the fit force constants. By giving the second contribution sufficient weight, only select terms were found to vary significantly.

The fit potential was tested by calculating the transition energies of CD_3O. Good agreement was found. We were unable to assign most of the low frequency fundamentals. The difficulties of making a normal mode assignment was elucidated through the use of a correlation diagram. To obtain these diagrams we plot the eigenvalues of the full Hamiltonian for which we have multiplied all Jahn-Teller and anharmonic vibrational contributions by a parameter that varies from 0 to 1. In this way the Hamiltonian continuously varies from the fully assignable spin-orbit coupled, normal mode Hamiltonian to the fully coupled Hamiltonian. The observed avoided crossings indicate that the zero-order picture is very different from the eigenstate representation. Analogous plots for CH_3O were obtained. Here there are many fewer avoided crossings and the spectrum can be assigned. The reasons for this difference were discussed.

We presented a procedure for calculating the dipole

moment expansion. This expansion is performed using a set of vibronic operators that have well defined transformation properties with respect to the threefold symmetry axis. The coefficients in this expansion were determined using the finite field approach as implemented by MOLPRO at the CCSD(T) level of theory.[41] The dipole expansions were used to calculate the IR spectrum of methoxy, paying particular attention to the spectrum in the region of the CH stretch. While the general features of the spectrum can be understood, making connections to experiment is not yet possible to the Fermi interactions with background states.

Appendix

In this Appendix we describe the calculation of the numerical values of the coefficients in eq 9. We do this by projecting this potential onto states that one can calculate *ab initio*. We then extend these ideas to the calculation of the dipole moment functions.

Using the definitions of the operators, eq 7, and bases, eq 6, we obtain

$$\begin{aligned}\langle A'|\mathscr{L}_\pm\mathscr{L}_\pm|A'\rangle &= \frac{1}{2},\\ \langle A''|\mathscr{L}_\pm\mathscr{L}_\pm|A''\rangle &= -\frac{1}{2}.\end{aligned} \tag{A.1}$$

Combining eq A.1 with the fact that, if we only consider motion along the coordinate S_x, we can set $S_y = 0$ in eq 1 to give $S_\pm = S_x$. With these projections eq 9 leads to

$$\begin{aligned}\langle V\rangle_{A'} \equiv \langle A'|V|A'\rangle &= \alpha S_x^2 + \beta S_x + \gamma S_x^2;\\ \langle V\rangle_{A''} \equiv \langle A''|V|A''\rangle &= \alpha S_x^2 - \beta S_x - \gamma S_x^2.\end{aligned} \tag{A.2}$$

The coefficients are obtained by calculating the energies of the two potentials for various values of S_x *ab initio* and then obtaining the expansion coefficients of eq A.2 via least squares fitting the sums and differences of these energies. Having calculated the coefficients, we can numerically evaluate the adiabatic potential energy at any specific value of $\{S_x, S_y\}$ by diagonalizing the 2×2 matrix representation of eq 9.

Although couched in a different language this is equivalent to the procedure implemented and tested in Paper I.[21] The advantage of the current approach is that we can extend it to calculate the dipole moment functions. This we now do.

The form of the dipole operator expansion can also be determined by symmetry. We find

$$\begin{aligned}\hat{C}_3\mu_\pm &= \exp[\pm i2\pi/3]\mu_\pm\\ \hat{C}_3\mu_z &= \mu_z\end{aligned} \tag{A.3}$$

where $\mu_\pm = \mu_x \pm i\mu_y$. Through first order these operators must take the form

$$\begin{aligned}\mu_z &= B_{00} + B_{11}\left[S_+\mathscr{L}_+\mathscr{L}_+ + h.c.\right]\\ \mu_+ &= A_{00}\mathscr{L}_-\mathscr{L}_- + A'_{11}S_+ + A_{11}S_-\mathscr{L}_+\mathscr{L}_+\\ \mu_- &= A_{00}\mathscr{L}_+\mathscr{L}_+ + A'_{11}S_- + A_{11}S_+\mathscr{L}_-\mathscr{L}_-.\end{aligned} \tag{A.4}$$

As $\mu_\pm$ are hermitian conjugates of each other, only results for the μ_+ operator will be given henceforth. Likewise, since μ_z transforms as the potential, we will not include it in further discussion. We have included it above both to highlight that this component has a contribution linear in the E-mode as well as to clarify the notation we employ in the dipole expansions. The first subscript of the coefficients refers to the order of the coordinate expansion, and the second subscript refers to the net change in vibrational angular momentum. In contrast to the z component, for the $\mu_\pm$ expansion there are two linear terms that change the vibrational angular momentum by one. We distinguish these two terms with a prime superscript, *e.g.* we have terms A_{11} and A'_{11}.

The second order contribution is

$$\begin{aligned}\mu_+^{(2)} = {} & A_{20}S_+S_-\mathscr{L}_-\mathscr{L}_- + A'_{22}S_-S_-\\ & + A_{22}S_+S_+\mathscr{L}_+\mathscr{L}_+\end{aligned} \tag{A.5}$$

The numerical values of the expansion coefficients are obtained following the same projection techniques that we used to obtain the potential of eq A.2. Using the $\mu_+^{(2)}$ operator as an example, we find for $S_y = 0$

$$\begin{aligned}\langle\mu_+^{(2)}\rangle_{A'} = \langle\mu_x^{(2)}\rangle_{A'} &= \left[\frac{A_{20}}{2} + A'_{22} + \frac{A_{22}}{2}\right]S_x^2,\\ \langle\mu_+^{(2)}\rangle_{A''} = \langle\mu_x^{(2)}\rangle_{A''} &= -\left[\frac{A_{20}}{2} - A'_{22} + \frac{A_{22}}{2}\right]S_x^2\end{aligned} \tag{A.6}$$

Taking the sums and differences of these expressions one obtains for all the terms through second order

$$\begin{aligned}\langle\mu_z\rangle_{A'} - \langle\mu_z\rangle_{A''} &= 2B_{11}S_x + 2B_{22}S_x^2\\ \langle\mu_z\rangle_{A'} + \langle\mu_z\rangle_{A''} &= 2B_{00} + 2B_{20}S_x^2\\ \langle\mu_x\rangle_{A'} - \langle\mu_x\rangle_{A''} &= A_{00} + A_{11}S_x + [A_{20} + A_{22}]\,S_x^2\\ \langle\mu_x\rangle_{A'} + \langle\mu_x\rangle_{A''} &= 2A'_{11}S_x + 2A'_{22}S_x^2.\end{aligned} \tag{A.7}$$

The left side values are calculated with the MOLPRO suite,[41] using the finite field approach, at the CCSD(T) level of theory and cc-pVTZ basis, for various displacements along S_x, and the results fit to a quadratic polynomial in order to obtain the coefficients. Note that in contrast to the potential, we are unable to resolve the individual values of the A_{20} and A_{22} terms, only their sum. The spectra reported in this paper are relatively insensitive to these quadratic terms.

ACKNOWLEDGMENTS

This material is based upon work supported by the National Science Foundation under Grant No. CHE-0911559.

* E–mail address: sibert@chem.wisc.edu

[1] Powers, D. E.; Pushkarsky, M. B.; Miller, T. A. *J. Chem. Phys.* **1997**, *106*, 6863–6877.

[2] Powers, D. E.; Pushkarsky, M. B.; Miller, T. A. *J. Chem. Phys.* **1997**, *106*, 6878–6884.

[3] Osborn, D. L.; Leahy, D. J.; Neumark, D. M. *J. Phys. Chem. A* **1997**, *101*, 6583–6592.

[4] Geers, A.; Kappert, J.; Temps, F.; Wiebrecht, J. W. *Ber. Bunsenges. Phys. Chem.* **1990**, *94*, 1219–1224.

[5] Geers, A.; Kappert, J.; Temps, F.; Wiebrecht, J. W. *J. Chem. Phys.* **1990**, *93*, 1472–1473.

[6] Han, J. X.; Utkin, Y. G.; Chen, H. B.; Burns, L. A.; Curl, R. F. *J. Chem. Phys.* **2002**, *117*, 6538–6545.

[7] Feng, L.; Demyanenko, A.; Reisler, H. *J. Chem. Phys.* **2003**, *118*, 9623–9628.

[8] Feng, L.; Wei, J.; Reisler, H. *J. Phys. Chem. A* **2004**, *108*, 7903–7908.

[9] Feng, L.; Demyanenko, A.; Reisler, H. *J. Chem. Phys.* **2004**, *120*, 6524–6530.

[10] Liu, J.; Chen, M. W.; Melnik, D.; Yi, J. T.; Miller, T. A. *J. Chem. Phys.* **2009**, *130*(7), 074302.

[11] Han, J.; Hu, S.; Chen, H.; Utkin, Y.; Brown, J.; Curl, R. *Phys. Chem. Chem. Phys.* **2007**, *9*(28), 3725 – 3734.

[12] Bent, G. D. *J. Chem. Phys.* **1994**, *100*, 8219–8232.

[13] Barckholtz, T. A.; Miller, T. A. *J. Phys. Chem. A* **1999**, *103*, 2321–2336.

[14] Marenich, A. V.; Boggs, J. E. *J. Chem. Phys.* **2003**, *119*, 10105–10114.

[15] Marenich, A. V.; Boggs, J. E. *Chem. Phys. Lett.* **2005**, *404*, 351–355.

[16] Geers, A.; Kappert, J.; Temps, F.; Sears, T. J. *J. Chem. Phys.* **1993**, *98*, 4297–4300.

[17] Schmidt-Klugmann.; J..; Koppel, H.; Schmatz, S.; Botschwina, P. *Chem. Phys. Lett.* **2003**, *369*, 21–30.

[18] Marenich, A. V.; Boggs, J. E. *J. Chem. Phys.* **2005**, *122*, 024308.

[19] Bent, G. D.; Adams, G. F.; Bartram, R. H.; Purvis, G. D.; Bartlett, R. J. *J. Chem. Phys.* **1982**, *76*, 4144–4156.

[20] Barckholtz, T. A.; Miller, T. A. *Int. Revs. in Phys. Chem.* **1998**, *17*, 435–524.

[21] Nagesh, J.; Sibert, E. L. *Phys. Chem. Chem. Phys.* **2010**, *12*(29), 8250–8259.

[22] Dillon, J.; Yarkony, D. R.; Schuurman, M. S. *J. Chem. Phys.* **2011**, *134*(18), 184314.

[23] Dillon, J.; Yarkony, D. R.; Schuurman, M. S. *J. Chem. Phys.* **2011**, *134*(4), 044101.

[24] Höpper, U.; Botschwina, P.; Köppel, H. *J. Chem. Phys.* **2000**, *112*, 4132.

[25] Hougen, J. T. *J. Molec. Spec.* **1980**, *81*, 73–92.

[26] Herzberg, G.; Van Nostrand Reinhold Company: New York, 1966; pages 40–48.

[27] Ramesh, S. G.; Sibert, E. L. *Mol. Phys.* **2005**, *103*, 149–162.

[28] Wilson, E. B.; Decius, J. C.; Cross, P. C. *Molecular Vibrations;* McGraw-Hill: New York, 1955.

[29] Endo, Y.; Saito, S.; Hirota, E. *J. Chem. Phys.* **1984**, *81*, 122.

[30] Longuet-Higgins, H.; Öpik, U.; Pryce, M.; Sack, R. A. *Proc. Roy. Soc. Lon. Series A, Math. Phys. Sci.* **1958**, *244*(1236), 1 – 16.

[31] Stanton, J. F. *Mol. Phys.* **2009**, *107*(8-12), 1059–1075.

[32] Davidson, E. R. *Rev. Mod. Phys.* **1972**, *44*, 451.

[33] Cullum, J. K.; Willoughby, R. A. *"Lanczos Algorithms for large symmetric eigenvalues computations";* Birkhäuser: Boston, 1985.

[34] Cullum, J. K., Willoughby, R. A., Eds. *Large scale eigenvalue problems: proceedings of the IBM Europe Institute Workshop on Large Scale Eigenvalue Problems held in Oberlech, Austria, July 8-12, 1985;* Elsevier, 1986.

[35] Wang, X.-G.; Carrington, T. *The Journal of Chemical Physics* **2004**, *121*(7), 2937–2954.

[36] Wang, X.-G.; Carrington, T. *The Journal of Chemical Physics* **2003**, *119*(1), 101–117.

[37] Temps, F.; World Scientific: Singapore, 1995; page 375.

[38] Foster, S.; Misra, P.; Lin, T.; Damo, C.; Carter, C.; Miller, T. *J. Phys. Chem.* **1988**, *92*(21), 5914–5921.

[39] Lee, Y.; Wann, G.; Lee, Y. *J. Chem. Phys.* **1993**, *99*(12), 9465–9471.

[40] Misra, P.; Zhu, X.; Hsueh, C.; Halpern, J. *Chem. Phys.* **1993**, *178*(1-3), 377–385.

[41] Molpro, version 2008.1, a package of ab initio programs. Werner, H.-J.; Knowles, P. J.; Lindh, R.; Manby, F. R.; Schütz, M.; others. **2008**.